Direct radiative forcing of Saharan dust in the Mediterranean from measurements at Lampedusa Island and MISR space-borne observations

D. Meloni[1] and A. di Sarra

Climate Laboratory, Ente per le Nuove Tecnologie, l'Energia e l'Ambiente, Rome, Italy

T. Di Iorio and G. Fiocco

Department of Physics, University "La Sapienza," Rome, Italy

[1] Ground-based observations were carried out at the island of Lampedusa, in the central Mediterranean, simultaneously to measurements of the Multiangle Imaging Spectro-Radiometer (MISR) instrument aboard the Terra satellite, in 2 days of July 2002 (14 and 16) when Saharan dust was present. Ground-based measurements include ultraviolet spectral irradiance; visible global and diffuse irradiances at several bands; aerosol optical depth in the ultraviolet, visible, and near infrared; aerosol backscattering; and depolarization profiles. The aerosol optical depth at 500 nm was very similar on both days (0.23). Large, irregular particles were present in the atmospheric layers between 2 and 6 km on 14 July and between 1 and 5 km on 16 July. According to backward trajectories, the airmasses arriving at Lampedusa spent a large fraction of the previous days over central Sahara on 14 July, while passing over northern Africa on 16 July. The different trajectories influence the value of the Ångström exponent, depolarization, and backscattering produced by aerosols. A significant increase of the aerosol optical depth in the ultraviolet is observed, and is attributed to steep variations of the particles' refractive index. A radiative transfer model is used to reconstruct the observed radiative fluxes at the surface and the radiance at the satellite altitude, and to estimate the direct aerosol radiative forcing in the $290-800$ nm and in the visible spectral range. The best agreement between measured and modeled radiative fluxes is found for values of the single scattering albedo of $0.96-0.97$ (14 July) and $0.88-0.89$ (16 July) and of the asymmetry parameter of $0.79-0.80$ (14 July) and $0.81-0.82$ (16 July), indicating that significantly different optical properties pertain to dust particles of different origin. The instantaneous direct radiative forcing per unit optical depth over the $400-700$ nm spectral interval is $-(39-79)$ W m^{-2} at the surface and $-(5-20)$ W m^{-2} at the top of the atmosphere. Although desert dust is the dominant aerosol type on both days, large differences, as large as a factor of 2 in the forcing efficiency at the surface and a factor of 3 at the top of the atmosphere, are found. Calculations were also performed to study the effect of nonspherical aerosol shapes by using different scattering phase functions, and comparing modeled and measured reflectivities at the nine observation angles of MISR. The different phase functions match the observed wavelength dependence of the aerosol optical depth and produce similar reflectance patterns for a scattering angle <150°. The effect of nonspherical particles becomes important mainly at scattering angles in the $150-180°$ interval. This effect should be taken into account in the derivation of radiation fluxes from satellite radiance measurements.   *INDEX TERMS:* 0305 Atmospheric Composition and Structure: Aerosols and particles (0345, 4801); 0360 Atmospheric Composition and Structure: Transmission and scattering of radiation; 3359 Meteorology and Atmospheric Dynamics: Radiative processes; 3360 Meteorology and Atmospheric Dynamics: Remote sensing; *KEYWORDS:* atmospheric aerosols, radiative forcing, dust, radiative transfer

---

[1]Also at Department of Physics, University "La Sapienza," Rome, Italy.

1. Introduction

[2] Aerosols are key components of the Earth's atmosphere. Their radiative effects have a substantial impact on both local and global energy budgets. The aerosol properties relevant to estimate their radiative effects are the optical depth, the single scattering albedo, and the phase function, which depend on the composition, size distribution, and shape of the particles, and consequently vary with wavelength and height. The estimate of the aerosol radiative effects is often based on the use of prescribed classes of aerosol types, published by several authors [*Shettle and Fenn*, 1979; *d'Almeida et al.*, 1991; *Hess et al.*, 1998]; these classes generally assume spherical particles with a lognormal size distribution and a complex refractive index. Aerosol properties may, however, significantly differ from the assumed aerosol classes because of the complexity of the production mechanisms, the characteristics of the sources, and the atmospheric processes that may affect them.

[3] Several field experiments have been conducted worldwide to measure or derive aerosol characteristics. For example, the Tropospheric Aerosol Radiative Forcing Observational Experiment (TARFOX) was aimed at reducing the uncertainties on the estimates of the radiative effects of summer haze in the eastern coast of the United States; TARFOX took place in July 1997 [*Russell et al.*, 1999]. The Indian Ocean Experiment (INDOEX) started in January and February 1996 to study the impact of anthropogenic aerosol transported from the Indian continent to the tropical Indian Ocean [*Ramanathan et al.*, 1996]. Other campaigns aimed at reducing the uncertainties in the estimates of aerosol radiative forcing were carried out recently in different regions of the globe. The Transport and Chemical Evolution over the Pacific (TRACE-P) mission conducted in April and May 2001 had as major objectives the understanding and quantification of the outflow of radiatively important gases and aerosols from the Asian continent to the western Pacific in spring [*Jacob et al.*, 2003]. The Aerosol Characterization Experiments (ACE-1 in the southwest Pacific Ocean in 1995 [*Bates et al.*, 1998], ACE-2 in the North Atlantic Ocean in 1997 [*Raes et al.*, 2000], and ACE-Asia off the coast of China, Japan, and Korea in spring 2001 [*Huebert et al.*, 2003]) gave an insight into the mechanisms through which aerosols influence the chemical and radiative properties of the atmosphere. During most of these campaigns, extensive measurements were carried out from multiple platforms (i.e., ground, ship, aircraft, satellite), and several "closure" experiments were conducted. A closure approach is applied when the aerosol properties are to be determined using a redundant set of radiometric quantities obtained by independent instruments or methods. In this type of studies the application of radiative transfer models is fundamental [*Formenti et al.*, 2002; *Silva et al.*, 2002].

[4] In the Mediterranean, different types of aerosols and mixtures of different kinds of particles may be found. Aerosols may vary from marine, continental, including athropogenic-polluted, and mineral. In winter, the Mediterranean is generally under the influence of northwesterly flow, and continental and marine particles are generally found over the basin. In summer, the Mediterranean is under the influence of the descending branch of the Hadley cell, and transport of desert dust from the Sahara is rather common. Within this general scheme, that produces a marked seasonal behavior of the aerosol optical depth [e.g., *Moulin et al.*, 1998], the aerosol distribution is modulated by the synoptic meteorological conditions [see, e.g., *di Sarra et al.*, 2001].

[5] A closure study was carried out in the Mediterranean in May and June 1999, by comparing ground-based and airborne measurements of aerosol properties [*Di Iorio et al.*, 2003] and using the derived information to reproduce measured ultraviolet, visible, and near-infrared radiation fluxes by means of a radiative transfer model [*Meloni et al.*, 2003a, 2003b]. The analysis has shown that significant differences between the observed and the climatological size distributions exist and that the use of climatological size distributions produces relatively large deviations from the observed surface irradiance. Large variations of the aerosol optical properties are found, and these variations are related to the origin of the airmasses and of the transported particles. The knowledge of the aerosol vertical distribution of desert dust is important, mainly for a correct estimate of the radiation profiles in the troposphere. On the basis of the observations and using the radiative transfer model, estimates of the aerosol direct radiative forcing were derived. The forcing efficiency (i.e., the direct radiative forcing per unit optical depth) is larger for continental/marine aerosol than for desert dust. Desert dust, however, produces a larger forcing, since dust transport is generally associated with large aerosol optical depths. The aerosol forcing at the top of the atmosphere, derived from the model calculations, was negative (i.e., inducing a cooling) for the desert dust case and close to zero or positive for continental particles. The upwelling flux at the top of the atmosphere was not measured during the experiment.

[6] In this paper we describe a closure experiment where ground-based measurements from an ultraviolet spectrophotometer, an aerosol lidar, and two Sun-photometers/radiometers (MFRSR), and space-borne observations from the Multiangle Imaging Spectro-Radiometer (MISR), are combined to derive column-integrated aerosol optical properties needed in radiative transfer calculations. The observations are carried at the Station for Climate Observations on the island of Lampedusa (35.5°N, 12.6°E) in the central Mediterranean Sea. In particular, this study is aimed at deriving the column-integrated values of the single scattering albedo, ω_0, and of the asymmetry factor, g, which best describe the aerosol properties on two days of July 2002, when airmasses originating from Africa and loaded by a moderate amount of desert dust (optical depth at 500 nm of about 0.23) reach Lampedusa. On both days the dust layer extends up to 5.5–6 km altitude.

[7] As a first step, the column-integrated values of ω_0 and g, which give the best agreement between measurements and model simulations, are determined: the best match

search is made over the MFRSR global irradiances and the MISR reflectances. The bands of the ground-based and the space-borne instruments differ both in the central wavelength and in bandwidth; thus wavelength-independent values for ω_0 and g are used as input in the radiative transfer model to reproduce the MFRSR irradiances and the MISR equivalent reflectances in their respective visible bands. Model simulations of the spectral ultraviolet irradiance are also performed. Finally, the model is applied to estimate the aerosol radiative forcing at the surface and at the top of the atmosphere. Such an estimate is constrained by the measured MISR radiances and takes advantage from the multiangle geometry of the instrument.

[8] The effects of different aerosol phase functions, describing in a qualitative manner the behavior of spherical and nonspherical particles, on the simulated equivalent reflectances are also investigated. Phase functions for spherical and nonspherical particles have different side and back scattering, thus influencing the estimate of the aerosol radiative forcing.

2. Observations and Methodology

2.1. Ground-Based Measurements

[9] The island of Lampedusa hosts the Laboratory for Climate Observations of the Ente per le Nuove Tecnologie, l'Energia e l'Ambiente (ENEA) of Italy, where a set of instruments is routinely operational; other instruments that require the direct control by dedicated operators are run only in selected periods. Lampedusa is a small (about 20 km^2) remote site in the Mediterranean, south of Sicily, relatively far from pollution sources. Its geographic characteristics make Lampedusa a good site for satellite data validation, since the island represents a small perturbation to the background ocean albedo. In July 2002, simultaneous measurements of aerosols, ozone, and radiation where carried out. The instrumentation included a (double monochromator) Brewer MK III spectrophotometer, a tropospheric aerosol lidar, and a visible (MFR-7) and an ultraviolet (UV-MFR-4) Multi Filter Rotating Shadowband Radiometer (MFRSR).

[10] The Brewer spectrophotometer measures total ozone with about 1% accuracy and spectral downward irradiance between 286.5 and 363 nm at 0.5 nm intervals with an estimated uncertainties of 4–5% [di Sarra et al., 2002]. The Brewer spectrophotometer irradiance measurements were calibrated by means of the NIST/NOAA portable field calibrator [Early et al., 1998], with several NIST traceable 1000 W FEL lamps in March 2002. The responsivity of the system was thereafter checked by means of 50 W halogen lamps.

[11] The lidar was developed at the University of Rome to measure aerosol backscattering and depolarization profiles at 532 nm throughout the troposphere in daytime conditions. The system was used in previous campaigns [e.g., di Sarra et al., 2001] and was upgraded in 2002 to expand the sounding interval toward lower altitudes by adding a refractive 50 mm aperture telescope that allows the retrieval of useful signals from above approximately 60–100 m.

[12] The visible and the ultraviolet MFRSR measure global and diffuse irradiances that are subtracted to derive direct radiation needed to calculate aerosol optical depths

(AOD) at various wavelengths [Harrison et al., 1994]; it has a broadband (350–1000 nm) channel and six narrowband channels with central wavelengths at 415.6, 495.7, 614.6, 672.8, 868.7, and 939.6 nm and about 10 nm full width at half maximum (FWHM) bandwidths. The UV-MFR-4 has four channels centered at 299.8, 305.4, 311.3, and 317.6 nm, with bandwidths of about 2 nm FWHM. The AODs at the visible MFRSR bands are calculated by calibrating the photometer with the Langley method, selecting for the calibration about 10 half days characterized by clear and stable atmospheric conditions. The AOD is calculated from the measurements after removing the contribution of molecular extinction, absorption by O_3 (for the bands at 495.7, 614.6, and 672.8 nm), and absorption by NO_2 (for the band centered at 415.6 nm). NO_2 correction is done using the column amount based on the Global Ozone Monitoring Experiment (GOME) data [Burrows et al., 1999a].

[13] The accuracy on the global irradiances can be estimated, taking into account the uncertainty on the extraterrestrial solar irradiance and on the instrumental extraterrestrial flux derived with the Langley method. Thuillier et al. [1998] show that different extraterrestrial solar spectra agree within 3%. Taking into account the uncertainties associated with the instrumental extraterrestrial flux, with the analog-to-digital conversion of the signal, and on the extraterrestrial irradiance, an overall accuracy of 3.2% on the global irradiance measured by the MFRSR is estimated, which corresponds to 0.04–0.05 W m^{-2}nm^{-1}, depending on the band.

[14] The extraterrestrial solar irradiance, weighted for the transmission curve of each MFRSR band, was derived by comparing the measured and modeled direct component of the downward flux. The differences of the extraterrestrial irradiances derived on the 2 days are smaller than 2%.

[15] The use of the Langley method is impractical for the UV-MFRSR owing to the large role played by ozone and its variations. The correction of the daily ozone variability, although in principle possible, would produce relatively large errors on the estimated extraterrestrial constant. Thus the UV-MFRSR was calibrated by comparing the measured global irradiances with those determined by the Brewer spectrophotometer. Initially, the Brewer spectra of 14 and 16 July are convoluted with the UV-MFRSR filter functions, assumed of Gaussian shape; then the UV-MFRSR measurements, performed every 3 min, are interpolated at the time of the Brewer UV scan. The ratio of the Brewer global irradiance and the UV-MFRSR signal for each channel, averaged over the central hours of each day, gives the UV-MFRSR calibration factor. This factor can be multiplied to the UV-MFRSR direct radiation signals (obtained as the global minus the diffuse) to derive calibrated irradiances. Finally, from the Beer-Lambert law the AOD is derived, knowing the extraterrestrial flux and after subtracting the Rayleigh and the absorbing gas contributions. The Rayleigh optical depth is calculated after Bucholtz [1995].

[16] On the basis of the broadband channel of the MFRSR, on the lidar data, and on visual observations at Lampedusa, 2 cloud-free days, 14 and 16 July 2002, when ground-based observations where simultaneous to the MISR passage above Lampedusa, were identified. Figure 1 shows
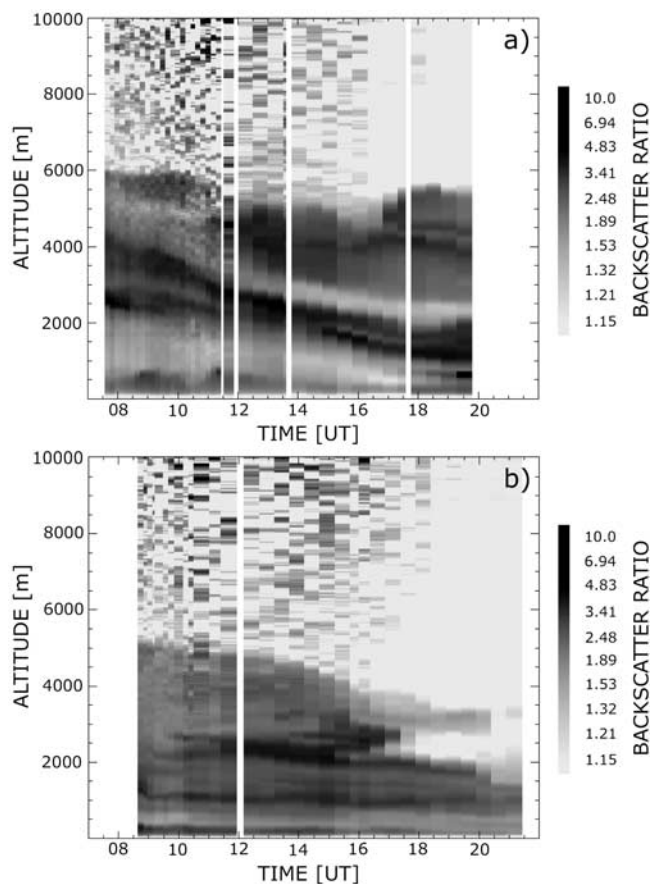
Figure 1. Evolution of the lidar backscatter ratio profiles for (a) 14 July and (b) 16 July.

the lidar backscatter ratio R (the ratio of the backscattering coefficient of aerosol and molecules to that of the molecules only) profiles derived from signals integrated over 10 min intervals, for the 2 days. R exceeds one when aerosols are present. The local time of the MISR overpass is 1208 on 14 July and 1155 on 16 July. On 14 July (Figure 1a) aerosols are detected up to 6 km, with largest values of the back-scatter ratio in the 2–4 km and 5–6 km layers. In Figure 2 the profile of the aerosol backscattering coefficient, β_a, closest in time to the satellite overpass is depicted, showing a maximum aerosol amount between 3 and 4 km. The reader is reminded that R is scaled to the backscattering produced by the molecules, while β_a, i.e., the backscattering cross section per unit volume, is, although in a complex way, more directly related to the aerosol concentration and mass.

[17] From the daytime lidar observations, taking into account the instrumental sensitivity, it is possible to exclude that that cirri with an optical depth >0.003 were present on the 2 days at the time of the satellite overpass. The influence of thinner cirri that might have been present on the 2 days was neglected in the analysis.

[18] To identify the origin of the airmasses arriving at Lampedusa on 14 and 16 July, backward trajectories were calculated by means of the HYSPLIT transport model [*Draxler and Rolph*, 2003], which uses meteorological model vertical velocity fields. Trajectories ending over the island at different altitudes at the time of the satellite overpass were calculated. Figure 3a shows that on 14 July

the airmass arriving at Lampedusa at 1 km originates from North, while the airmasses at 2 and 3 km were over Morocco 5–7 days earlier, flowed afterwards toward southern Spain and Italy, spent the last 2 days over North-Western Libya and over the Mediterranean, and reached Lampedusa from South. The airmasses arriving at Lampedusa at 4–6 km spent most of the last 6–7 days over Africa, running South of the Atlas Mountains, then over North-Western Libya, Tunisia, and reaching Lampedusa from South West. This pattern finds a striking correspondence in the backscattering profile (Figure 2), that has a minimum in the region 0.8–1.5 km altitude range, corresponding to the trajectory that does not pass over Africa, and higher values in the above layers, up to 5–6 km. On 16 July the airmasses arriving at Lampedusa at altitudes between 1 and 6 km follow a similar path (Figure 3b), reaching the island roughly from West, after spending only the last 1–2 days over Africa (North Algeria and Tunisia). The values of R and β_a are lower on 16 July than on 14 July throughout the region 2–6 km. The opposite occurs in the region 0.7–2 km. It must be noted that in this altitude range the airmass did not pass over Africa on 14 July, while on 16 July also the trajectory ending at 1 km passed over North Africa. As shown by *di Sarra et al.* [2001] the aerosol backscatter ratio is generally larger for trajectories that spend a long time over Africa.

[19] Table 1 shows the aerosol optical depths at 415.6 and 868.7 nm averaged in a 1 hour interval around the time of the satellite overpass, derived from the visible MFRSR measurements and the retrieved Ångström parameters, α and β, according to the formula

$$AOD(\lambda) = \beta\lambda^{-\alpha}. \tag{1}$$

[20] The values of AODs on the 2 days are similar. It is worth noticing that these values are in the lower limit of the range previously observed during Saharan dust events at
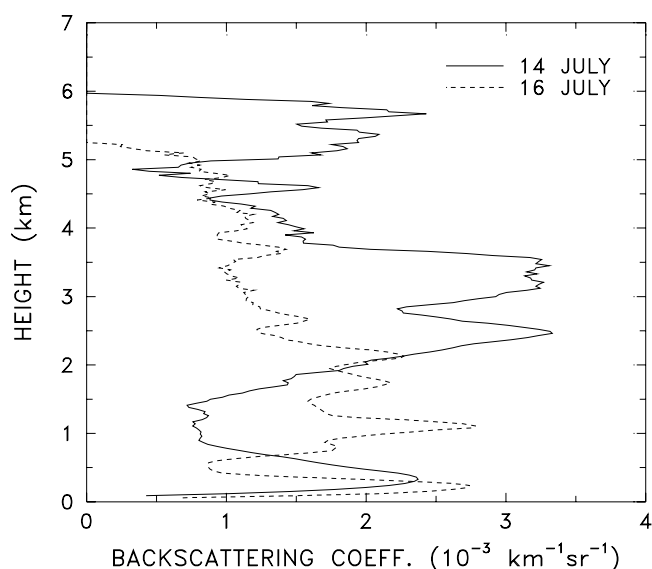

Figure 2. Lidar backscattering coefficient profiles for 14 July (solid line) and 16 July (dashed line) at the time of the MISR overpass.
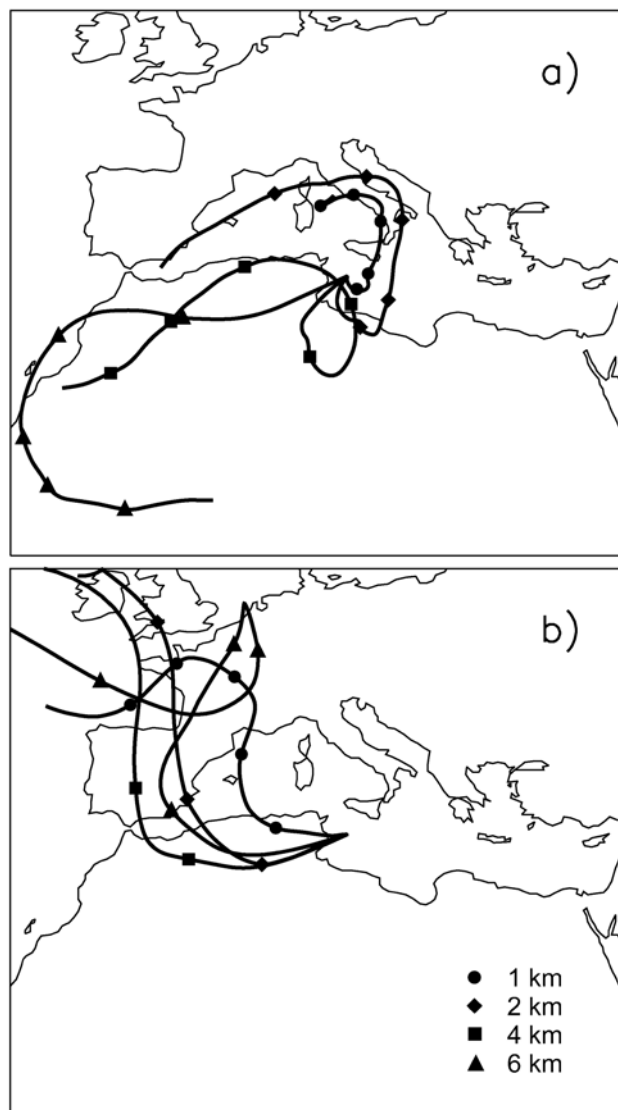
Figure 3. Isentropic backward trajectories at various heights ending at Lampedusa on (a) 14 July and (b) 16 July.

Lampedusa [see, e.g., *di Sarra et al.*, 2002; *Di Iorio et al.*, 2003]. The Ångström exponent provides information about the particles' size: in both cases α is relatively small, meaning that there is a component of large size aerosols which has dominant optical properties. The different trajectories, the characteristics of the source regions, and the longer time of residence over Africa probably produced airmasses containing larger particles on 14 July than on 16 July. The presumably stronger convective activity associated with the part of the trajectory spent over Africa may also have played a role.

[21] The aerosol depolarization provides an indication of the particle shape: values close to zero are expected for spherical particles, and higher values are produced by nonspherical particles [*Reagan et al.*, 1989]. The average aerosol depolarization (defined as the ratio between the aerosol backscattered signal components with polarization perpendicular and parallel to the laser linear polarization,

respectively) over three different layers of the cloud has been calculated from the lidar measurements averaged over 1 hour interval around the time of the satellite overpass. The lidar configuration does not allow retrieval of the aerosol depolarization below about 1.5 km. On 14 July the average depolarization (and its standard deviation) was 0.46 ± 0.14 for the $1.35-4.8$ km layer and 0.56 ± 0.09 between 4.8 and 6 km. These rather high values confirm that large asymmetrical particles from the Sahara were present on 14 July. On 16 July the average depolarization values were 0.47 ± 0.09 in the layer $0.45-2.4$ km and 0.25 ± 0.07 between 2.4 and 5.1 km, indicating somewhat distinct properties in the two layers.

2.2. Satellite Data

[22] The MISR instrument [*Diner et al.*, 1998] was launched aboard the Terra spacecraft on December 1999. It has been designed to view the Earth's atmosphere in nine different directions in order to detect the angular variation of the sunlight reflected by clouds, aerosols, and the surface. MISR nine cameras (CCDs) are arranged in the following configuration: a nadir viewing camera (identified as AN), a group of four cameras pointing in the forward direction (AF, BF, CF, and DF with increasing off-nadir angle), and a group of four cameras pointing in the afterward direction (AA, BA, CA, DA). The fore and aft cameras are displaced in a symmetrical arrangement with respect to the nadir camera, with nominal viewing angles of 26.1, 45.6, 60.0, and 70.5°. Each camera images the underlying scene in four spectral bands centered at 446.4, 557.5, 671.7, and 866.4 nm with bandwidths of 41.9, 28.6, 21.9, and 39.7 nm, respectively. The time interval between the observation of a point on the surface by the DF and DA cameras is 7 min.

[23] Onboard calibration is performed monthly by multiple in-flight methodologies, using solar-reflecting diffuse panels, detector standards, and a goniometer to verify that there is no degradation in the reflectance shape of the panels. In addition, semiannual overflight field campaigns are conducted. A 3% absolute radiometric uncertainty at the maximum signal is estimated [*Diner et al.*, 1998].

[24] The 705 km orbit of the Terra satellite is near-polar and Sun-synchronous, with a 1030 LT equator crossing time on the descending node and a global coverage repeat cycle of 16 days, corresponding to 233 orbits. The swath width has been designed to be 360 km so that the coverage of a latitude circle is achieved every 9 days at the equator and every 2 days at the poles.

[25] The cross-track dimension of a pixel is 275 m for the off-nadir cameras and 250 m for the nadir camera, while the sample spacing in the along-track direction is 275 m in all cameras. Typically, MISR observes the Earth at a lower resolution, obtained averaging the adjacent samples, so that only the nadir camera acquires images with all four bands at 275 m resolution (1×1 pixels), while the other eight cameras produce data at 275 m resolution in the red band,

Table 1. Aerosol Optical Depth (AOD) Measured by the MFRSR at 415.6 and 868.7 nm and the Derived Ångström Parameters

Day	AOD (415.6 nm)	AOD (868.7 nm)	α	β
14/07/2002	0.230 ± 0.002	0.217 ± 0.001	0.080	0.215
16/07/2002	0.259 ± 0.001	0.155 ± 0.002	0.698	0.140

Table 2. Geometric Parameters Corresponding to the MISR Observations on 14 and 16 July

Camera	14/07/2002 Solar Zenith Angle = 20.09° Solar Azimuth Angle = 308.42°				16/07/2002 Solar Zenith Angle = 22.38° Solar Azimuth Angle = 303.77°			
	Viewing Zenith Angle	Viewing Azimuth Angle	Scattering Angle	Glitter Angle	Viewing Zenith Angle	Viewing Azimuth Angle	Scattering Angle	Glitter Angle
DF	70.06	11.93	100.15	62.34	70.90	21.13	102.93	67.59
CF	59.95	10.75	109.41	52.53	61.00	24.42	113.22	59.84
BF	45.63	8.05	122.19	38.66	47.46	30.37	127.49	50.08
AF	26.55	0.18	138.17	20.75	30.31	44.32	146.46	40.27
AN	7.87	282.58	152.62	13.43	15.99	102.21	170.54	37.69
AA	27.49	212.33	148.20	35.28	29.29	164.03	161.56	48.37
BA	46.34	204.89	134.95	53.83	46.63	178.85	142.51	61.55
CA	60.55	202.20	123.04	67.78	60.51	185.01	127.94	72.80
DA	70.81	200.93	113.97	77.80	70.62	188.29	117.48	81.24

while the remaining channels are averaged at 1.1 km resolution (4 × 4 pixels).

[26] Our analysis will try to take advantage of the good radiometric accuracy and the multiangle viewing geometry of MISR. The estimate of the TOA fluxes is based, for most satellite instruments, on the observations of the radiance in a single direction. The measurements at several viewing angles provided by MISR give the opportunity to attempt a more detailed reconstruction of the outgoing radiation scattered by the Earth atmosphere and surface. Moreover, the multiangle geometry may be used to derive some atmospheric properties (in particular, it may provide information on the aerosol phase function), at the same time reducing the number of assumptions on the atmospheric structure needed to estimate the TOA fluxes for example through a radiative transfer model.

[27] We used the calibrated, coregistered, and geolocated MISR radiances for the 36 channels (nine viewing angles for four wavelengths) at 1.1 km sampling. The geometric parameters, that is the solar zenith and azimuth angles, and the viewing zenith and azimuth angles for each of the nine cameras at the time of the satellite passage over Lampedusa are reported in Table 2.

[28] For our purpose, the MISR radiances have been averaged over all the pixels occupied by the sea included in the area between 35.4° and 35.6° latitude N and between 12.4° and 12.75° longitude E, excluding the pixels that correspond to the island surface: a total of 538 and 539 pixels have been used in the averages for 14 and 16 July, respectively. The MISR radiances are converted into equivalent reflectances with the formula

$$\rho(i,k) = \frac{L(i,k) \cdot \pi \cdot d^2}{E_0(i)}, \tag{2}$$

where is the radiance measured in the i band by the k camera, d is the Earth-Sun distance in AU, and $E_o(i)$ is the extraterrestrial solar irradiance in the i band. The uncertainty associated to the reflectances can be estimated taking into account the standard deviation of the radiance averaged over the integrating area and the uncertainties associated to the absolute radiometric, relative pixel-to-pixel, band-to-band, and camera-to-camera responses [Bruegge et al., 1999], which have been evaluated from the in-flight calibration performed in June 2002. The radiance values for 14 July vary over the MISR pixels within 0.3 and 1%

(depending on the camera viewing angle) in the blue band, in the range 0.9–3% in the green and 1.8–4.3% in the red. For 16 July the ranges are 0.3–0.9% in the blue, 1.2–2.8% in the green, and 2.3–2.8 % in the red band. The resulting total relative uncertainty varies between 3 and 5%, the highest values being for the red band and the cameras at the smallest viewing angles; the band-weighted exoatmospheric irradiance measured by the MISR has uncertainties that can be neglected with respect to the other terms.

[29] A preliminary check aimed at removing radiance measurements contaminated by Sun glint was carried out. In the MISR retrieval algorithm a region is potentially glitter-contaminated when the glitter angle is lower than 30° [Diner et al., 1999]. On 14 July the AF and AN cameras measurements where contaminated by Sun glint (see Table 2), and only the remaining seven cameras are used in the analysis. No influence of Sun glint was detected on 16 July.

2.3. Model

[30] The UVSPEC model [Mayer et al., 1997] is based on the discrete ordinate method by Stamnes et al. [1988] for a plane-parallel atmosphere; a pseudo-spherical approximation [Dahlback and Stamnes, 1991] can be used for high solar zenith angles, when a correction to the photon path length is needed. The atmosphere is divided in stratified layers, each one of homogeneous composition, while optical properties change from layer to layer. The extraterrestrial solar spectrum is derived from Atlas 3 for wavelengths between 280 and 407.8 nm, from Atlas 2 between 407.8 and 419.9 nm, and from the Modtran 3.5 model in the 419.9–800 nm region [Kylling et al., 1998].

[31] The underlying surface is assumed to be Lambertian, and a wavelength-dependent albedo is assigned. Ozone is the only absorbing gas considered within the spectral range of validity for the model (280–800 nm); absorption bands of other atmospheric constituents, like NO_2, H_2O, or O_2, exist in this spectral range, and differences between model simulations and observations are expected in correspondence. Spectral radiance and irradiance can be computed at arbitrary wavelength steps and at each level between the ground and the TOA. The model inputs are the Sun position (zenith and azimuth angles), the zenith and azimuth viewing angles (in the radiance simulation), total ozone, vertical profiles of pressure, temperature, air density, and ozone. The aerosol characteristics are described by spectral single scattering albedo, ω_0, asymmetry factor, g, and extinction

coefficient at each level. We have applied the model to cloud-free cases. Several changes were made to the original model by *Mayer et al.* [1997], mainly to provide a more detailed description of the aerosol properties and atmospheric vertical structure. The implemented changes are described by *Meloni et al.* [2003a].

[32] The temperature-dependent ozone cross sections by *Burrows et al.* [1999b] are used in the model. In our version of the model the atmosphere is described by 64 layers of different thickness: 150 m from 0 to 2 km, 300 m from 2 to 8 km, and higher thicknesses for increasing heights. The pressure, temperature, and air density profiles are from the National Centers for Environmental Prediction (NCEP) analyses at 1200 GMT and are assumed not to vary from the MISR overpass to 1200 GMT. The pressure profile is scaled to the value measured by the sensor of the meteorological station of the laboratory. The climatological mid-latitude profiles derived by *Bhartia et al.* [1985] from solar backscatter ultraviolet (SBUV) and balloon observations are adapted by scaling the total ozone to the Brewer measurement.

[33] The vertical aerosol extinction profile has been derived from the lidar backscattering profile at 532 nm, multiplying β_a by the extinction-to-backscatter ratio e, which is a critical parameter in the retrieval of the backscattering profile from the lidar measurements. We have derived the ratio e applying the procedure described by *Di Iorio et al.* [2003], combining the lidar and the photometric measurements. The values of e, which give extinction profiles reproducing the AODs measured at ground by the MFRSR, are 20.0 sr and 26.3 sr for 14 and 16 July, respectively. It is worth noting that a lower value for the day with a higher content of Saharan dust, 14 July, is expected, as also reported by *Di Iorio et al.* [2003]. As discussed by *Meloni et al.* [2003a, 2003b], the knowledge of the aerosol vertical distribution is particularly important in the desert dust events. In these cases the aerosol vertical profile differs significantly from the assumed climatology generally used in radiative transfer models, and may impact the estimated radiation fluxes.

[34] The spectral aerosol optical depth values in the visible are calculated through the Ångström formula using the coefficients in Table 1, which have been determined from the AODs at 415.6 and 868.7 nm. The spectral albedo of the sea is independent from the surface roughness for high Sun, as is our case; in the UV the sea albedo ranges from 0.05 to 0.09 [*Doda and Green*, 1980]. *Payne* [1972] gives the shortwave albedo of the ocean: we have assumed a wavelength-independent value of 0.06 in the visible according to the solar zenith angle closest to the time of the satellite overpass.

[35] The radiance simulations are performed with 16 streams to give an accurate description of the photon paths through the atmosphere. Six streams are used to calculate the irradiance.

[36] Given the asymmetry factor g, the model uses the Henyey-Greenstein (HG) aerosol phase function, for which the n-order moment of the expansion in Legendre polynomials (the quantity used in the discrete ordinate method for the solution of the transfer equation) is known to be g^n. The HG phase function may be taken only as an approximation of the real aerosol phase function, particularly because it misses information for nonspherical particles. However, there is an important advantage in using the HG phase function: relevant parameters, such as the asymmetry parameter g and the single scattering albedo ω_0, may be derived without knowing (or assuming) aerosol size distribution and composition, as is our case. We assume that the derivation of these parameters by matching measured and modeled irradiances and radiances constitutes a reasonable constraint also on the HG phase function that depends on these parameters.

[37] Data, as well as air trajectories, suggest that different aerosol components may be present on the 2 days (i.e., a mixture of dust particles and background aerosols, which plausibly may contain sea salt particles and/or sulfates). In particular, different types of particles (marine aerosols in the lowest layer, desert dust above) were probably present on 14 July. On both days, dust largely constitutes the dominant aerosol fraction. It must be emphasized that also the distribution and composition of desert dust may significantly vary, depending on the characteristics of the source regions, intensity of the mobilization process and of the convection, time of travel, etc. The values of g and ω_0 that we retrieve from the analysis should thus be considered as "optically equivalent" parameters that include the influence of a nonhomogeneous vertical aerosol distribution and different aerosol properties on the 2 days. In paragraph 3.3 we examine the effect of different aerosol phase functions, for both spherical and nonspherical particles, on the reflectance pattern as a function of the scattering angle.

3. Results and Discussion

3.1. Simulations of Ground-Based Irradiance and Satellite Radiances

[38] The radiative transfer model is limited to an upper wavelength of 800 nm, and the measurements in the near-infrared channels are not used in the present analysis. Absorption by gases other than ozone can be neglected in the four MFRSR bands at shorter wavelengths (415.6, 495.7, 614.6, and 672.8 nm), being the NO_2 levels according to GOME data low.

[39] To derive information on the aerosol properties on 14 and 16 July, we performed model simulations varying ω_0 and g between 0.4 and 1.0 at 0.01 steps. For each day we computed the root mean square difference (RMSD), defined as

$$\text{RMSD} = \sqrt{\frac{1}{4} \sum_{i=1}^{4} \Delta^2(i)}, \qquad (3)$$

with

$$\Delta(i) = 100 \cdot \frac{I^s(i) - I^m(i)}{I^m(i)}, \qquad (4)$$

where $I^m(i)$ and $I^s(i)$ are the measured and simulated irradiances, respectively, in the i band. The two MFRSR measurements closest to the time of the satellite overpass are chosen and temporally interpolated. Figure 4 shows the plots of the RMSDs: the 3.2% threshold value is highlighted. This threshold delimits a region of values of ω_0 and
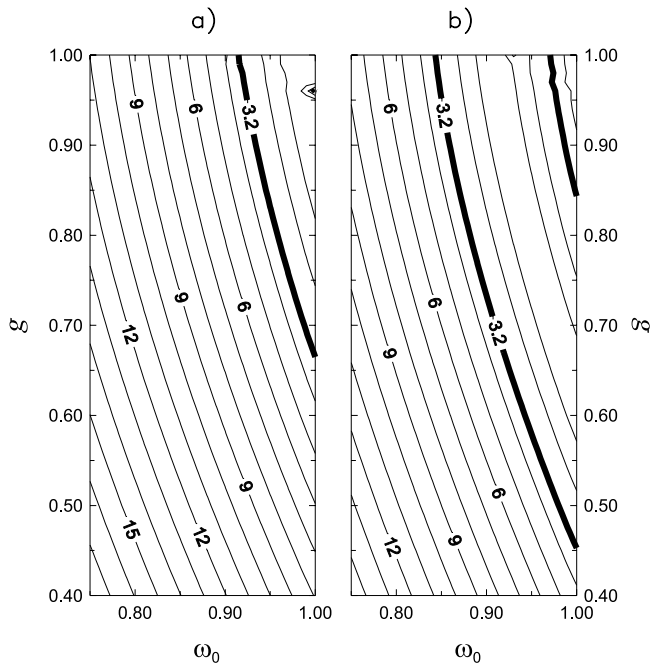
Figure 4. Plots of the RMSD between measured and modeled MFRSR irradiances for (a) 14 July and (b) 16 July. The thick curve indicates the 3.2% measurement uncertainty.

g that produce simulated global irradiances within the measurement uncertainties. On 14 July, ω_0 varies between 0.90 and 1.00 and *g* varies between 0.66 and 1.00, while on 16 July, ω_0 is in the range 0.84–1.00 and *g* is in the range 0.45–1.00.

[40] The same analysis is then applied to the MISR reflectivity. For MISR observations we define the RMSD as

$$\text{RMSD} = \sqrt{\frac{1}{3}\frac{1}{K}\sum_{i=1}^{3}\sum_{k=1}^{K}\Gamma^2(i,k)}, \qquad (5)$$

with

$$\Gamma(i,k) = 100 \cdot \frac{\rho^s(i,k) - \rho^m(i,k)}{\rho^m(i,k)}, \qquad (6)$$

where $\rho^m(i,k)$ and $\rho^s(i,k)$ are the measured and simulated equivalent reflectances defined in equation (1), respectively, in the *i* band for the *k* camera. The sum in expression (5) is performed on all the MISR cameras, excluding those affected by Sun glint. Figure 5 presents the plots of the RMSD on the 2 days. Minima of RMSD are higher than 10%; this difference is primarily due to discrepancies between model and observations in the green and red bands. To identify best values of ω_0 and *g*, we overlap the regions of minimum RMSD derived for the MFRSR irradiances and the MISR reflectances (i.e., where the RMSD of the global irradiances at the surface is <3.2%, and the RMSD of the MISR reflectances is <11% on 14 July and <13% on 16 July). The retrieved pairs of (ω_0, *g*) responding to these criteria are (0.96,0.80), (0.97,0.79), (0.97,0.80) on 14 July and (0.88,0.81), (0.88,0.82), (0.89,0.81), (0.89,0.82) on

16 July. The absolute minima of the RMSDs occur for ω_0 = 0.96 and *g* = 0.80 on 14 July and for ω_0 = 0.88 and *g* = 0.81 on 16 July.

[41] Few studies deal with the optical properties of desert dust in the Mediterranean. *Kouvarakis et al.* [2002] report a value of ω_0 = 0.87 at 532 nm for the dust episodes collected at Crete in May 1999 during the Photochemical Activity and Solar Ultraviolet Radiation (PAUR II) campaign. *Di Iorio et al.* [2003] and *Meloni et al.* [2003a] retrieved the column averaged ω_0 and *g* of the desert dust from data collected at Lampedusa island during PAUR II, using different approaches. Comparing the measured aerosol size distribution with the lidar-derived backscattering profile, *Di Iorio et al.* [2003] found ω_0 = 0.75 and *g* = 0.79 at 532 nm. Through the application of a radiative transfer model,
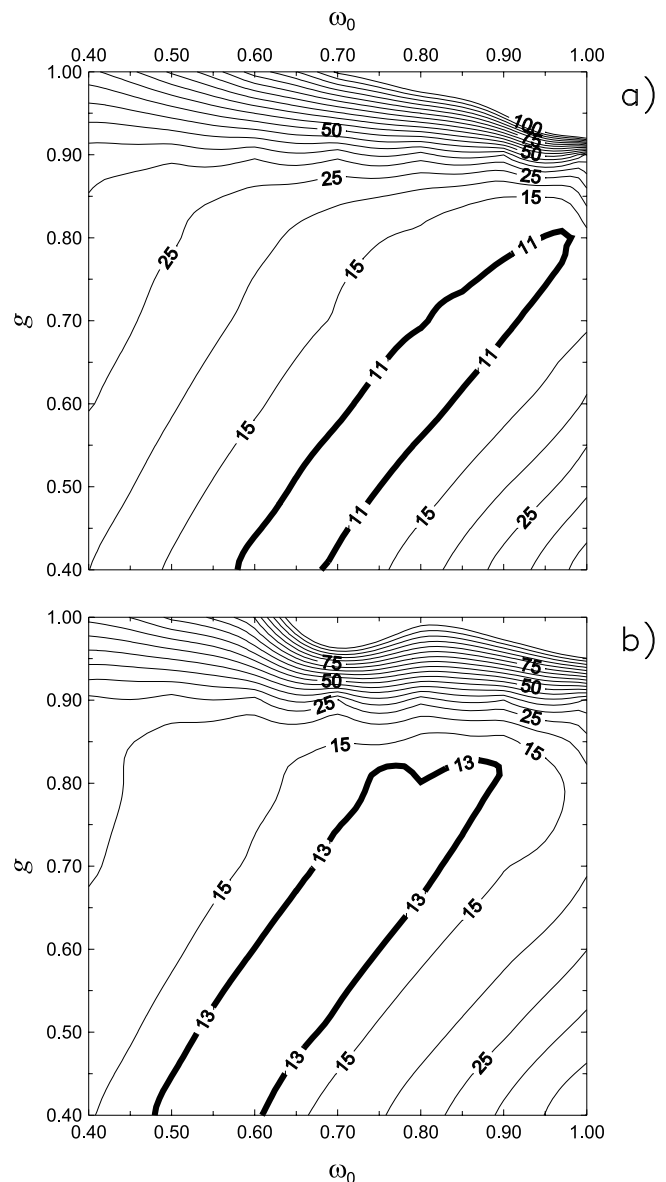

Figure 5. Plots of the RMSD between measured and modeled MISR equivalent reflectances for (a) 14 July and (b) 16 July. The thick curves show the regions with lowest RMSDs.
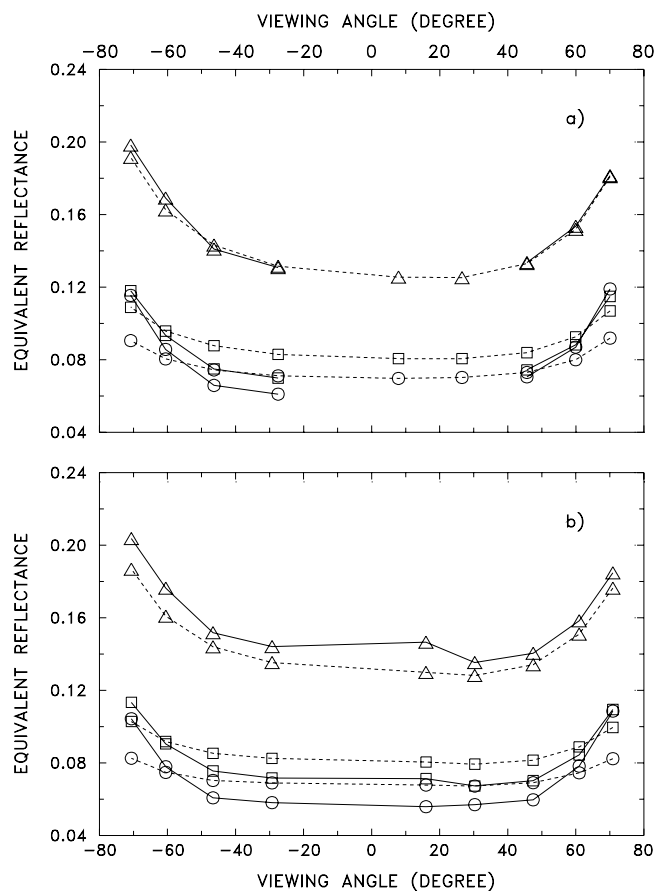
Figure 6. Modeled (dashed lines) and measured (solid lines) MISR equivalent reflectances as a function of the viewing zenith angle for (a) 14 July ($\omega_0 = 0.96$ and $g = 0.80$) and (b) 16 July ($\omega_0 = 0.88$ and $g = 0.81$). Triangles, squares, and circles identify measured reflectances in the blue, the green, and the red bands, respectively.

Meloni et al. [2003a] determined the wavelength-dependent ω_0 and g that best reproduce the measured UV spectral irradiance; the estimated values at 500 nm for the desert dust are in the range 0.73–0.84 and in the range 0.75–0.79, respectively. The main findings of the studies conducted worldwide on the dust optical characteristics have been summarized by *d'Almeida et al.* [1991] and, more recently, by *Dubovik et al.* [2002].

[42] Figure 6a shows the comparison between satellite and calculated equivalent reflectances as a function of the camera viewing angle for 14 July, when the glitter-contaminated AF and AN cameras have been excluded. The shape of both measurement and model curves is characterized by a higher signal at the further off-nadir cameras (DF and DA) due to the larger atmospheric airmasses. A good agreement is achieved in the blue band (2.1% RMSD) at all camera angles, while a model overestimate (up to 15%) is present in the green and red channels. Model underestimates measurements at the DF and DA cameras in the green band by 7 and 8%, respectively, and at the DF, CF, CA, and DA cameras in the red band, with differences of −23, −8, −6, and −22%.

[43] On 16 July (Figure 6b) the MISR blue radiance is underestimated by the model, with differences as large as 11% for the AN camera. Similarly to 14 July, on 16 July the model overestimates the space-borne measurements in the green band, except for the DF and DA cameras, and in the red band, except for the DF, CF, CA, and DA cameras.

[44] In the radiative transfer model we used a wavelength-dependent surface albedo and assumed a Lambertian surface. A different treatment of the surface albedo may possibly produce smaller differences between modeled and measured reflectivities. The use of a more complex surface albedo would however require further assumptions and would add a degree of arbitrariety.

[45] The wavelength-independent best values of ω_0 and g were used to reproduce with the model the Brewer
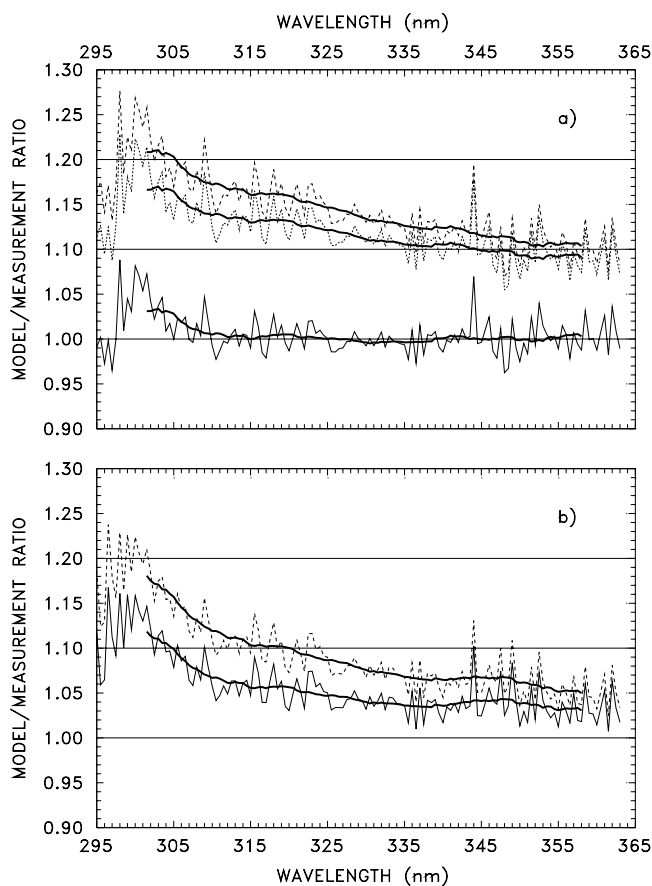

Figure 7. Ratio of the modeled and measured UV spectra for (a) 14 July and (b) 16 July, at the time of the satellite overpass. For Figure 7a the two dashed curves, from top to bottom, represent the ratios obtained with aerosol optical depth estimated from coefficients α and β of Table 1 and Table 3, respectively, and $\omega_0 = 0.96$ and $g = 0.80$; the solid curve is obtained with $\omega_0 = 0.78$ and $g = 0.80$ and optical depth derived from coefficients α and β of Table 3 (see text). For Figure 7b the two curves, from top to bottom, represent the ratios obtained with aerosol optical depth estimated with coefficients α and β of Table 1 and in Table 3, respectively. The thick solid curves are 10-nm running averages of the ratio.

Table 3. Aerosol Optical Depth (AOD) Measured by the UV-MFR-4 at 317.6 nm and by the MFRSR at 415.6 nm and the Derived Ångström Parameters

Day	AOD (317.6 nm)	AOD (415.6 nm)	α	β
14/07/2002	0.432 ± 0.005	0.230 ± 0.002	2.336	0.030
16/07/2002	0.474 ± 0.004	0.259 ± 0.001	2.250	0.036

spectral irradiances measured at the solar zenith angles of the MISR observations. The spectral model-to-measurement ratio for 14 and 16 July is shown in Figure 7; the thick lines are 10-nm running averages of the ratio. As a first case, we assume that the aerosol optical depth in the UV may be derived from the Ångström formula, using the coefficients α and β derived from optical depth measurements in the visible (Table 1). In this case, model results exceed measurements (i.e., the modeled irradiances are larger than observations), with differences between 11 and 21% for 14 July (Figure 7a) and between 5 and 18% for 16 July (Figure 7b).

[46] As a second case, we apply the Ångström formula using the coefficients α and β derived from optical depth measurements at 317.6 nm and 415.6 nm (Table 3). In this case the coefficients α and β are quite similar for the 2 days. It is worth noting that the values of α in Table 3 are much larger than those in Table 1, indicating a change in the aerosol optical properties with wavelength. A steep increase of the aerosol optical depth of Saharan dust in the UV was also observed by *Cattrall et al.* [2003], who performed Sun-photometric measurements from Dry Tortugas island (24.6°N, 82.9°W) in July and August 1998. The dust refractive index, mostly its imaginary part, strongly increases in the UV [see, e.g., *d'Almeida et al.*, 1991], possibly producing a significant increase of the optical depth. Part of this increase may also be due to a different composition of the smaller particles, to which UV wavelengths are more sensitive than visible wavelengths.

[47] Consequently, the radiative effects of the desert dust aerosol in the UV [*di Sarra et al.*, 2002] may be larger than what may be expected from measurements of the aerosol optical depth in the visible spectral range. Using the relatively large values of the optical depth in the UV estimated with the parameters of Table 3, the model simulation for 14 July still gives an overestimate of 9–16%, while for 16 July the 10-nm average of the model/measurement ratio oscillates around 1.03–1.05 (the model overestimates measurements by 3–5%) for wavelengths larger than 320 nm and is up to 1.12 below 310 nm. It is worth noting that the differences larger on 14 July than on 16 July indicate that on the first date aerosols were characterized by a stronger wavelength dependence of ω_0 and g.

[48] As a third case, we have performed model simulations for 14 July, fixing the asymmetry parameter at 0.80 and varying ω_0 in order to determine the value for which the model/measurement ratio is closest to 1; a value of $\omega_0 = 0.78$ produces differences between 0 and +3%. Thus a decrease of the single scattering albedo in the UV is needed to reproduce the measured irradiance. This result confirms that the optical properties of desert dust change significantly in the UV. The change is more

evident on 14 than on 16 July. As noted by *d'Almeida et al.* [1991], the single scattering albedo of desert dust is expected to increase with wavelength.

[49] In the radiative forcing calculations, reported in the next section, we used the values of ω_0 and g retrieved in the visible, since the Brewer spectral range (290–360 nm) contributes by 6–8% and 3–9% to the radiative forcing at ground and the TOA, respectively, depending on the examined days. Thus we neglected the influence of the behavior of the single scattering albedo in the UV on the radiative forcing.

3.2. Radiative Forcing

[50] The aerosol direct radiative forcing (RF) is the change in the radiation flux produced by the aerosols. At the ground level we define the RF as the net (downward minus upward) irradiance for an atmosphere with aerosol minus that for an aerosol-free atmosphere. At the TOA the RF is defined as the upward irradiance without aerosol minus that with aerosols: negative values mean that a larger fraction of the incoming radiation is reflected back to space when aerosols are present. We calculate the RF between 290 and 800 nm, integrating the modeled spectral irradiances and using the pairs of ω_0 and g previously derived. Table 4 reports the results for the 2 days. As expected, at the ground aerosols produce a reduction of the radiation with respect to the aerosol-free case; conversely, at the TOA the presence of aerosol particles induces an increase of the portion of incident radiation that is scattered back to space. The difference between the two days is remarkable although the solar zenith angles and the AODs are very close: on 16 July the RF at the surface is significantly higher and at the TOA is lower than that on 14 July. This difference is attributed to the higher absorption and the lower backscattering for the aerosol of 16 July, in accordance with the retrieved values of ω_0 and g. The reader is reminded that desert dust on both days was the dominant aerosol component. Dust originating from different source regions may show different optical properties and largely different radiative effects.

[51] The variations of the aerosol optical properties with altitude may affect the results we obtain. It is, however, not possible to derive information on the vertical distribution of the aerosol optical properties from the available measurements. An analysis of the influence of different aerosol properties at different altitudes would require a large number of assumptions on their size distribution and composition. We have preferred to use the available constraints provided by the observations to derive column-integrated optical parameters, whose effects are similar to those produced by the more complex real situation.

Table 4. Instantaneous Aerosol Radiative Forcing, RF, at the Surface and at the Top of the Atmosphere (TOA), Calculated by Integrating the Simulated Spectra Over the Spectral Range 290–800 nm

Day	ω_0	g	Instantaneous RF, W m^{-2}	
			Surface	TOA
14/07/2002	0.96–0.97	0.79–0.80	−(12.3–13.9)	−(5.3–6.2)
16/07/2002	0.88–0.89	0.81–0.82	−(23.1–25.0)	−(1.2–1.9)

Table 5. Instantaneous Aerosol Forcing Efficiency, RFE, (Per Unit AOD at 500 nm) at the Surface and at the Top of the Atmosphere (TOA) Calculated Between 400 and 700 nm

Day	ω_0	g	Instantaneous RFE, W m^{-2}	
			Surface	TOA
14/07/2002	0.96–0.97	0.79–0.80	−(39.3–44.2)	−(17.3–20.1)
16/07/2002	0.88–0.89	0.81–0.82	−(73.2–79.0)	−(5.1–7.4)

On the considered days, desert dust (although originating from different regions of North Africa) is the dominant component of the aerosol over the column.

[52] On July 14 the back-trajectories and the stratification in the lidar profile indicate a neat distinction between the aerosols respectively below and above 1.5 km, and this case was selected to investigate the influence of the presence of two layers with distinct properties. On the basis of the available measurements, we can derive the aerosol concentration profile, but we have to assume the composition and dimension of the aerosol in the lowest layer, which can be reasonably constituted by sea salt and water-soluble particles. We assumed aerosol particles of maritime-polluted type between 0 and 1.5 km, with $\omega_0 = 0.96$ and $g = 0.69$ at 500 nm [d'Almeida et al., 1991], and a layer of dust-like particles between 1.5 and 6 km. We have searched for the layer 1.5–6 km (i.e., for the desert dust only) the values of ω_0 and g that minimize the difference between modeled and measured global irradiances and equivalent reflectances. For this layer we found $\omega_0 = 0.96$ and $g = 0.82$. We examined the differences in the aerosol radiative forcing between the two cases. Considering two different aerosol layers instead of one gives negligible differences in the RF at the surface between 290 and 800 nm (+1.3%) and a +3% difference at the TOA.

[53] Most works dealing with Saharan dust have been performed to evaluate the TOA RF in the shortwave (SW) region of the solar spectrum. For a comparison with RF in the visible, we can reasonably assume that the visible represents about 40% of the SW radiation. *Ackerman and Chung* [1992] used Earth Radiation Budget Experiment (ERBE) satellite data to study the effects of dust on the radiative SW fluxes at the TOA. They found that in a case of dust outbreak in the Saudi Arabian peninsula during July 1985 the RF ranged between 40 and 90 W m^{-2}. *Hsu et al.* [2000] determined the shortwave monthly average TOA RF due to Saharan dust in the eastern Atlantic; using a combination of TOMS and ERBE data they found that in July 1985 the averaged dust forcing was 40–50 W m^{-2}. In order to compare our results with previous works, we have calculated the radiative forcing efficiency (RFE) in the visible, that is, the radiative forcing between 400 and 700 nm per unit of AOD at 500 nm. The obtained values are reported in Table 5, but it worth reminding that these are instantaneous values and can sensibly differ from the daily or monthly averages. A summary of the main results of some intensive field campaigns for different types of aerosols can be found in the work of *Meloni et al.* [2003a].

[54] The solar zenith angle at the time of the satellite overpass is very close on the 2 days, and a direct comparison of the MISR radiances for each band is possible. The radiances of 14 July in the green and red bands are higher than those of 16 July, while the opposite occurs for the blue band. This behavior is consistent with the derived AOD spectral behavior: the AOD in the blue band, as well as the upwelling radiance, is higher on 16 July, while in the green and red bands (those which mainly control the visible RF) the AOD and the upwelling radiance are higher on 14 July.

3.3. Sensitivity on the Aerosol Phase Function

[55] As stated in paragraph 2.3, the modeled radiances are obtained using the Henyey-Greenstein (HG) phase function for the aerosols. With the aim of studying the sensitivity of the simulated radiances to different phase functions, we have considered spherical and nonspherical particles. It is worth stressing that the following analysis is qualitative and is meant to examine how the various phase functions reproduce the MISR radiance pattern as a function of the scattering angles. The effects of nonspherical particle shape on the aerosol retrieval and on the satellite radiances have been widely studied [e.g., *Mishchenko et al.*, 1995; *Kahn et al.*, 1997; *Tanré et al.*, 2001; *Müller et al.*, 2003]. In the following analyses we will assume the same single scattering albedo derived in the previous sections; this assumption is somehow crude, since the phase functions depends on the refractive index and on the single scattering albedos. Nevertheless, it is beyond the purpose of this paper a complete investigation of the effect of combined changes of phase function and optical attenuation of desert dust, and we will not vary the value of ω_0.

[56] For spherical particles (SP), we started from the size distribution of 18 May 1999, an episode of Saharan dust outbreak at Lampedusa that was examined by *Di Iorio et al.* [2003] and *Meloni et al.* [2003a]. Di Iorio et al. determined the column-averaged three-modal aerosol size distribution combining particle size, lidar, and photometric measurements (see Figure 3a of their paper), while Meloni et al. used the retrieved size distribution as input in a radiative transfer model and found the wavelength-independent refractive index which best reproduced the measured UV irradiances at the ground, under the assumption of the Mie theory, i.e., spherical shape and homogeneous composition. Since the Ångström parameter α on 18 May 1999 was different from the values found in July 2002, we have balanced the three modes of the size distribution of 18 May 1999 to reproduce the AOD measured on 14 and 16 July 2002 at 418.6 and 868.7 nm and thus the Ångström parameter α. To do so, we considered the contribution to the aerosol optical depth at 415.6 nm and 868.7 nm from the first two modes of the size distribution (median radii of 0.07 and 1.24 μm) and the contribution of the third mode (median radius 5.3 μm) and we searched the mixing ratios which allowed to obtain the measured AODs. The calculation was made applying the Mie theory and using the refractive index of $1.536 - 0.0044i$ found on 18 May 1999. Finally, the aerosol phase function was calculated at 532 nm and assumed not to vary with wavelength. The results are reported as solid curves in Figures 8d and 8h. Substantial differences were found on the 2 days, with a larger fraction of big particles on 14 July than on 16 July: the effective radii of these new size distributions are 4.35 μm for 14 July and 0.99 μm for 16 July. The resulting asymmetry factor g is 0.85 on 14 July and 0.69 on 16 July, far from that found in the reflectance simulations with HG phase function for 14 July ($g = 0.80$) and for 16 July ($g = 0.81$).
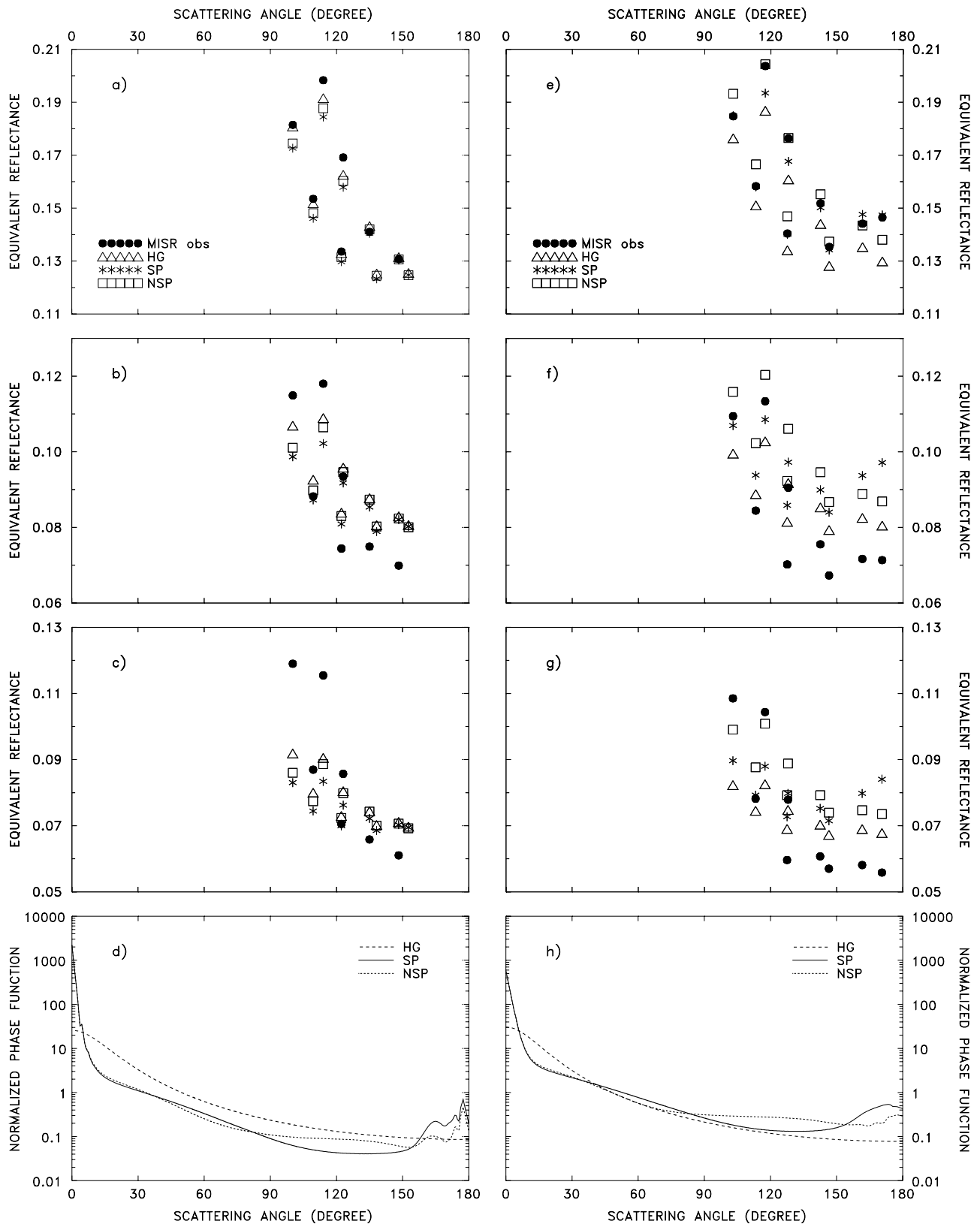
Figure 8. Equivalent reflectances in the blue, green, and red (from top to bottom) MISR bands simulated using different phase functions (d–h) (see text) versus scattering angle for 14 July (left panels) and 16 July (right panels). Measurements are also shown (solid circles).

[57] In order to obtain a phase function which reproduces the features of nonspherical particles (NSP), i.e., a higher side scattering (at scattering angles, θ, between approximately 90° and 150°) and a lower backscattering ($\theta > 150°$), we have adopted the ratio of the nonspherical to spherical phase functions reported by *Mishchenko et al.* [1997] for dustlike type particles at wavelength 443 nm; the authors consider a size distribution of polydisperse and randomly oriented prolate and oblate spheroids, with the maximum radius for the equivalent sphere (the sphere with the same projected area as that of the spheroid) of 2 μm. It must be emphasized that the dust size distribution often, and also in our case, contains a significant amount of particles larger than 2 μm. Calculations made for spheroids with a size distribution that includes particles up to 15 μm of radius produce similar results with respect to the same distribution of spheres [*Müller et al.*, 2003]. An accurate description of the phase function of nonspherical particles would require the detailed knowledge of their shape (and composition) and a complex treatment of their interaction with the radiation. Given the large number of assumptions that have to be made, the determination of the optical behavior of nonspherical dust particles is inherently qualitative. In the following analyses we will assume that the behavior described by *Mishchenko et al.* [1997] provides a sufficient description of the effect of the nonsphericity.

[58] The value of the asymmetry factor g for the NSP phase function is 0.86 for 14 July and 0.65 for 16 July; these values are not far from those obtained on the two days with the SP phase function. The impact of the HG, SP, and NSP phase functions on the equivalent reflectances is reported in the left (14 July) and right (16 July) panels of Figure 8 as a function of the scattering angle. The SP phase function has a minimum between 100° and 150°; the HG curve is above the SP and NSP phase functions for $\theta < 160°$ on 14 July, while it is below the SP and NSP for $\theta > 80°$ on 16 July.

[59] On both days the three phase functions HG, SP, and NSP reproduce the reflectance patterns for $\theta < 150°$. On 14 July the best reflectance pattern is given by the HG phase function in the blue band. On 16 July the simulated reflectances in the blue obtained using the SP phase function reproduce the patterns of the measured quantities at all scattering angles, included the highest one. In the other two bands the reflectance patterns are not reproduced neither by the spherical or the nonspherical particles' phase function for both days: this would indicate that, first of all, the changes of the phase function with the wavelength should be taken into account. Moreover, in the green and red bands the differences between the reflectances at the lowest and highest scattering angles are larger for the measurements than for the simulations.

[60] It should be noted that on 16 July the MISR AN camera (viewing zenith angle of 16° and scattering angle of 170.5°) measures equivalent reflectances in the blue band higher that those of the near AF and AA cameras (see Figure 6b). This behavior may be due to a possible influence of Sun glints, or the dependence on the scattering angle may be attributed to the differences of the phase function around the backward direction: the HG and the NSP phase functions are rather flat between 150 and 170°

and cannot reproduce the AN peak; the SP function, with a more pronounced backscattering, gives conversely highest reflectances in the AN and AA directions.

4. Conclusions

[61] In this work, visible and ultraviolet irradiances measured at ground and reflectances measured from space during transport of desert dust over the Mediterranean are reconstructed and analyzed with a radiative transfer model. Ground-based measurements that include aerosol backscattering and depolarization profiles by lidar were performed at the island of Lampedusa in 2 days of July 2002, simultaneously to the observations by the MISR instrument aboard the Terra spacecraft. The backward trajectories of 14 July indicate that the airmass spent a few days over the central Sahara before arriving at Lampedusa, while on 16 July the airmass originated from North Atlantic and ended at Lampedusa after passing over the northern margin of Algeria and Tunisia. The Ångström parameter and the aerosol depolarization reveal the presence of large particles of irregular shape on both days; the Ångström parameter is lower and the depolarization higher on 14 July, suggesting a strong impact of the passage over central Sahara. Differences in the aerosol vertical distribution are also observed, with most of the dust located between 2 and 6 km on 14 July and between 1 and 5 km on 16 July.

[62] A detailed radiative transfer model was applied to reproduce the spectral radiation measurements both at ground and from space, with the aim of deriving information about the aerosol properties. The main results of this study may be summarized as follows:

[63] 1. The wavelength-independent ω_0 and g in the visible which reproduce the irradiance measurements at ground and the reflectance observations from the satellite have been estimated: ω_0 ranges between 0.96 and 0.97 on 14 July and between 0.88 and 0.89 on 16 July; g varies in the range 0.79–0.82 for both days. On 16 July ω_0 is smaller than on 14 July: this may reflect a different chemical composition of the particles in the 2 days, with the aerosol on 16 July containing a larger amount of absorbing substances. This result show that dust optical properties may be significantly different, possibly depending on the characteristics of the source region.

[64] 2. The MISR equivalent reflectances measured at nine viewing angles on the 2 days have been simulated by the model, using the aerosol optical parameters α and β and the best match ω_0 and g ($\omega_0 = 0.96$ and $g = 0.80$ for 14 July and $\omega_0 = 0.88$ and $g = 0.81$ for 16 July), previously obtained. Since no information about the aerosol phase functions is available, the Henyey-Greenstein function is used in the model. The equivalent reflectances in the blue band are well reproduced on both days, while in the green and red bands the model overestimates the reflectance at the viewing angles closest to the nadir and underestimates the measurements at the steeper viewing angles, where the signal is more effectively affected by the presence of aerosols.

[65] 3. The observed optical depth shows a sudden increase in the ultraviolet spectral range. The Ångström exponent calculated using the optical depth at 317.6 nm is significantly larger (around 2.3) than the one obtained in the

visible. Values of the single scattering albedo lower than in the visible, down to 0.78, are needed to reproduce with the model the observed UV spectral irradiances measured by the Brewer spectrometer on 14 July.

[66] 4. The aerosol radiative forcing has been estimated at the surface and at the TOA in the 290–800 nm spectral range. On both days aerosols produce a reduction of the downward radiative flux at the surface and an increase of the outgoing flux at the TOA. The forcing efficiency at the surface is larger for the airmass of 16 July, while the aerosol of 14 July is more effective in reflecting the incoming radiation back to space, as expected from the ω_0 and g values. The instantaneous direct radiative forcing efficiency integrated over the 400–700 nm spectral range is between -39 and -79 W m^{-2} at the surface and between -5 and -20 W m^{-2} at the top of the atmosphere. The optical properties of the desert dust thus strongly influence the radiative forcing, and a detailed characterization of the aerosol properties is needed to derive a reliable estimate of the radiative effects.

[67] 5. Two different phase functions were used to study their influence on the equivalent reflectances pattern. The phase functions were derived from an assumed size distribution matching the observed optical depths at different wavelengths, for spherical and nonspherical particles. The influence of non-spherical particles is largest when scattering angles in the 150–180° range are sounded by MISR (16 July). Our results show that the shape of the phase function plays a significant role when trying to retrieve the aerosol radiative impact from a single radiance measurement.

References

Ackerman, S. A., and H. Chung (1992), Radiative effects of airborne dust on regional energy budgets at the top of the atmosphere, *J. Appl. Meteorol.*, 31, 223–241.

Bates, T. S., B. J. Huebert, J. L. Gras, F. B. Griffiths, and P. A. Durkee (1998), International Global Atmospheric Chemistry (IGAC) project's 1st Aerosol Characterization Experiment (ACE 1) overview, *J. Geophys. Res.*, 103, 16,297–16,318.

Bhartia, P. K., D. Silberstein, B. Monosmith, and A. J. Fleig (1985), Standard profiles of ozone from ground to 60 km obtained by combining satellite and ground based measurements, in *Atmospheric Ozone*, edited by C. S. Zerefos and A. Ghazi, pp. 243–247, D. Reidel, Norwell, Mass.

Bruegge, C. J., D. J. Diner, R. P. Korechoff, and M. Lee (1999), MISR Level 1 radiance scaling and conditioning algorithm theoretical basis, *JPL D-11507, Rev. E*, Jet Propul. Lab., Pasadena, Calif.

Bucholtz, A. (1995), Rayleigh-scattering calculations for the terrestrial atmosphere, *Appl. Opt.*, 34, 2765–2773.

Burrows, J. P., et al. (1999a), The Global Ozone Monitoring Experiment (GOME): Mission concept and first scientific results, *J. Atmos. Sci.*, 56, 151–175.

Burrows, J. P., A. Dehn, B. Deters, S. Himmelmann, A. Richter, S. Voigt, and J. Orphal (1999b), Atmospheric remote-sensing reference data from GOME: 2. Temperature-dependent absorption cross sections of O_3 in the 231–794 nm range, *J. Quant. Spectrosc. Radiat. Transfer*, 61, 509–517.

Cattrall, C., K. L. Carder, and H. R. Gordon (2003), Columnar aerosol single-scattering albedo and phase function retrieved from sky radiance over the ocean: Measurements of Saharan dust, *J. Geophys. Res.*, 108(D9), 4287, doi:10.1029/2002JD002497.

Dahlback, A., and K. Stamnes (1991), A new spherical model for computing the radiation field available for photolysis and heating at twilight, *Planet. Space Sci.*, 39, 671–683.

d'Almeida, G. A., P. Koepke, and E. P. Shettle (1991), *Atmospheric Aerosols Global Climatology and Radiative Characteristics*, A. Deepak, Hampton, Va.

Di Iorio, T., A. di Sarra, W. Junkermann, M. Cacciani, G. Fiocco, and D. Fuà (2003), Tropospheric aerosols in the Mediterranean: 1. Microphysical and optical properties, *J. Geophys. Res.*, 108(D10), 4316, doi:10.1029/2002JD002815.

Diner, D. J., et al. (1998), Multi-angle Imaging SpectroRadiometer (MISR) instrument description and experiment overview, *IEEE Trans. Geosci. Remote Sens.*, 36, 1072–1087.

Diner, D. J., L. Di Girolamo, and E. E. Clothiaux (1999), MISR Level 1 cloud detection algorithm theoretical basis, *JPL D-13397, Rev. B*, Jet Propul. Lab., Pasadena, Calif.

di Sarra, A., T. Di Iorio, M. Cacciani, G. Fiocco, and D. Fuà (2001), Saharan dust profiles measured by lidar at Lampedusa, *J. Geophys. Res.*, 106, 10,335–10,348.

di Sarra, A., M. Cacciani, P. Chamard, C. Cornwall, J. J. DeLuisi, T. Di Iorio, P. Disterhoft, G. Fiocco, D. Fuà, and F. Monteleone (2002), Effects of desert dust and ozone on the ultraviolet irradiance at the Mediterranean island of Lampedusa during PAUR II, *J. Geophys. Res.*, 107(D18), 8135, doi:10.1029/2000JD000139.

Doda, D. D., and A. E. S. Green (1980), Surface reflectance measurements in the UV from an airborne platform. Part 1, *Appl. Opt.*, 19, 2140–2145.

Draxler, R. R., and G. D. Rolph (2003), HYSPLIT (HYbrid Single-Particle Lagrangian Integrated Trajectory) model, NOAA Air Resour, Lab., Silver Spring, Md. (Available at http://www.arl.noaa.gov/ready/hysplit4.html)

Dubovik, O., B. Holben, T. F. Eck, A. Smirnov, Y. J. Kaufman, M. D. King, D. Tanré, and I. Slutsker (2002), Variability of absorption and optical properties of key aerosol types observed in worldwide locations, *J. Atmos. Sci.*, 59, 590–608.

Early, E. E., E. A. Thompson, and P. Disterhoft (1998), Field calibration unit for ultraviolet spectroradiometers, *Appl. Opt.*, 37, 6664–6670.

Formenti, P., et al. (1998), STAAARTE-MED 1998 summer airborne measurements over the Aegean Sea: 2. Aerosol scattering and absorption, and radiative calculations, *J. Geophys. Res.*, 107(D21), 4451, doi:10.1029/2001JD001536.

Harrison, L., J. Michalsky, and J. Berndt (1994), Automated multifilter rotating shadow-band radiometer: an instrument for optical depth and radiation measurements, *Appl. Opt.*, 33, 5118–5125.

Hess, M., P. Koepke, and I. Schult (1998), Optical properties of aerosols and clouds: The software package OPAC, *Bull. Am. Meteorol. Soc.*, 79, 831–844.

Hsu, N. C., J. R. Herman, and C. Weaver (2000), Determination of radiative forcing of Saharan dust using combined TOMS and ERBE data, *J. Geophys. Res.*, 105, 20,649–20,661.

Huebert, B. J., T. Bates, P. B. Russell, G. Shi, Y. J. Kim, K. Kawamura, G. Carmichael, and T. Nakajima (2003), An overview of ACE-Asia: Strategies for quantifying the relationships between Asian aerosols and their climatic impacts, *J. Geophys. Res.*, 108(D23), 8633, doi:10.1029/2003JD003550.

Jacob, D. J., J. Crawford, M. M. Kleb, V. S. Connors, R. J. Bendura, J. L. Raper, G. W. Sachse, J. Gille, L. Emmons, and J. C. Heald (2003), Transport and chemical evolution over the Pacific (TRACE-P) mission: Design, execution, and first results, *J. Geophys. Res.*, 108(D20), 9000, doi:10.1029/2002JD003276.

Kahn, R., R. West, D. McDonald, B. Rheingans, and M. I. Mishchenko (1997), Sensitivity of multiangle remote sensing observations to aerosol sphericity, *J. Geophys. Res.*, 102, 16,861–16,870.

Kouvarakis, G., Y. Doukelis, N. Mihalopoulos, S. Rapsomanikis, J. Sciare, and M. Blumthaler (2002), Chemical, physical, and optical characterization of aerosols during PAUR II experiment, *J. Geophys. Res.*, 107(D18), 8141, doi:10.1029/2000JD000291.

Kylling, A., A. F. Bais, M. Blumthaler, J. Schreder, C. S. Zerefos, and E. Kosmidis (1998), Effect of aerosols on solar UV irradiances during the Photochemical Activity and Solar Ultraviolet Radiation campaign, *J. Geophys. Res.*, 103, 26,051–26,060.

Martonchik, J. V., D. J. Diner, R. A. Kahn, T. P. Ackerman, M. M. Verstaete, B. Pinty, and H. R. Gordon (1998), Techniques for the retrieval of aerosol properties over land and ocean using multiangle imaging, *IEEE Trans. Geosci. Remote Sens.*, 36, 1212–1227.

Mayer, B., G. Seckmayer, and A. Kylling (1997), Systematic long-term comparison of spectral UV measurements and UVSPEC modeling results, *J. Geophys. Res.*, 102, 8755–8767.

Meloni, D., A. di Sarra, J. DeLuisi, T. Di Iorio, G. Fiocco, W. Junkermann, and G. Pace (2003a), Tropospheric aerosols in the Mediterranean: 2. Radiative effects through model simulations and measurements, *J. Geophys. Res.*, *108*(D10), 4317, doi:10.1029/2002JD002807.

Meloni, D., A. di Sarra, G. Fiocco, and W. Junkermann (2003b), Tropospheric aerosols in the Mediterranean: 3. Measurements and modeling of actinic radiation profiles, *J. Geophys. Res.*, *108*(D10), 4323, doi:110.1029/2002JD003293.

Mishchenko, M. I., A. A. Lacis, B. E. Carlson, and L. D. Travis (1995), Nonsphericity of dust-like tropospheric aerosols: Implications for aerosol remote sensing and climate modeling, *Geophys. Res. Lett.*, *22*, 1077–1080.

Mishchenko, M. I., L. D. Travis, R. A. Kahn, and R. A. West (1997), Modeling phase functions for dustlike tropospheric aerosols using a shape mixture of randomly oriented polydisperse spheroids, *J. Geophys. Res.*, *102*, 16,831–16,847.

Moulin, C., et al. (1998), Satellite climatology of African dust transport in the Mediterranean atmosphere, *J. Geophys. Res.*, *103*, 13,137–13,144.

Moulin, C., H. R. Gordon, V. F. Banzon, and R. H. Evans (2001), Assessment of Saharan dust absorption in the visible from SeaWiFS imagery, *J. Geophys. Res.*, *106*, 18,239–18,249.

Müller, D., I. Mattis, U. Wandinger, A. Ansmann, D. Althausen, O. Dubovik, S. Eckhardt, and A. Stohl (2003), Saharan dust over a central European EARLINET-AERONET site: Combined observations with Raman lidar and Sun photometer, *J. Geophys. Res.*, *108*(D12), 4345, doi:10.1029/2002JD002918.

Payne, R. E. (1972), Albedo of the sea surface, *J. Atmos. Sci.*, *29*, 959–970.

Raes, F., T. Bates, F. McGovern, and M. Van Liedekerke (2000), The 2nd Aerosol Characterization Experiment (ACE-2): General overview and main results, *Tellus, Ser. B*, *52*, 111–125.

Ramanathan, V., et al. (1996), Indian Ocean Experiment (INDOEX), *C4 Rep.*, Scripps Inst. of Oceanogr., Univ. of Calif., San Diego, La Jolla, Calif.

Reagan, J. A., M. P. McCormick, and J. D. Spinhirne (1989), Lidar sensing of aerosols and clouds in the troposphere and stratosphere, *Proc. IEEE*, *77*, 433–447.

Russell, P. B., P. V. Hobbs, and L. Stowe (1999), Aerosol properties and radiative effects in the U.S. East coast haze plume: An overview of the Tropospheric Aerosol Radiative Forcing Observational Experiment (TARFOX), *J. Geophys. Res.*, *104*, 2213–2222.

Shettle, E. P., and R. W. Fenn (1979), Models of the aerosol of the lower atmosphere and the effects of humidity variations on their optical properties, *Rep. AFL-TR-79-214*, *Environ Res. Pap. 675*, Air Force Geophys. Lab., Bedford, Mass.

Silva, A. M., M. L. Bugalho, M. J. Costa, W. von Hoyningen-Huene, T. Schmidt, J. Heintzenberg, and S. Henning (2002), Aerosol optical properties from columnar data during the second Aerosol Characterization Experiment on the south coast of Portugal, *J. Geophys. Res.*, *107*(D22), 4642, doi:10.1029/2002JD002196.

Stamnes, K., S.-C. Tsay, W. Wiscombe, and K. Jayaweera (1988), Numerically stable algorithm for discrete-ordinate-method radiative transfer in multiple scattering and emitting layered media, *Appl. Opt.*, *27*, 2502–2509.

Tanré, D., Y. J. Kaufman, B. N. Holben, B. Chatenet, A. Karnieli, F. Lavenu, L. Blarel, O. Dubovik, L. A. Remer, and A. Smirnov (2001), Climatology of dust aerosol size distribution and optical properties derived from remotely sensed data in the solar spectrum, *J. Geophys. Res.*, *106*, 18,205–18,217.

Thuillier, G., M. Hersé, P. C. Simon, D. Labs, H. Mandel, and D. Gillotay (1998), Observation of the solar spectral irradiance from 200 nm to 870 nm during ATLAS 1 and ATLAS 2 missions by the SOLSPEC spectrometer, *Metrologia*, *35*, 689–695.

———————————

T. Di Iorio and G. Fiocco, Department of Physics, University "La Sapienza," Piazzale A. Moro 2, Roma 00185, Italy.

A. di Sarra and D. Meloni, Climate Laboratory, Ente per le Nuove Tecnologie, l'Energia e l'Ambiente, Via Anguillarese 301, 00060 S. Maria di Galeria, Italy. (daniela.meloni@casaccia.enea.it)